Colloid and Polymer Science (2020) 298:681–696
https://doi.org/10.1007/s00396-020-04654-z

INVITED ARTICLE

Rheology of colloidal and metallic glass formers

Thomas Voigtmann[1] · Miriam Siebenbürger[2] · Christian P. Amann[3] · Stefan U. Egelhaaf[4] · Sebastian Fritschi[5] · Matthias Krüger[6] · Marco Laurati[4,7] · Kevin J. Mutch[4] · Konrad H. Samwer[6]

Received: 3 February 2020 / Revised: 30 March 2020 / Accepted: 1 April 2020 / Published online: 26 April 2020

Abstract

Colloidal hard-sphere suspensions are convenient experimental models to understand soft matter, and also by analogy the structural-relaxation behavior of atomic or small-molecular fluids. We discuss this analogy for the flow and deformation behavior close to the glass transition. Based on a mapping of temperature to effective hard-sphere packing, the stress–strain curves of typical bulk metallic glass formers can be quantitatively compared with those of hard-sphere suspensions. Experiments on colloids give access to the microscopic structure under deformation on a single-particle level, providing insight into the yielding mechanisms that are likely also relevant for metallic glasses. We discuss the influence of higher-order angular signals in connection with non-affine particle rearrangements close to yielding. The results are qualitatively explained on the basis of the mode-coupling theory. We further illustrate the analogy of pre-strain dependence of the linear-elastic moduli using data on PS-PNiPAM suspensions.

Keywords Rheology · Colloidal suspensions · Metallic alloys

Introduction

Well-characterized Brownian colloidal dispersions with deliberately tuned interactions serve as invaluable model systems on two accounts: they are models of more complex suspensions that are of application interest in their own right and at the foundation of the field of soft-matter physics. On the other hand, the large size of the colloids (in the range of 10 nm to about 1 μm) implies that the relevant length and time scales match those accessible in visible-light spectroscopy and microscopy as well as those of human observers. Hence, colloidal suspensions serve as model systems of atomic and small-molecular systems, where the link between microscopic processes and macroscopic material behavior is much harder to study experimentally.

This "colloids as big atoms" paradigm [1, 2] is rooted in the observation that for a classical many-particle system, the kinetic degrees of freedom can be integrated out separately in the calculation of thermodynamic averages. Further integration over the solvent degrees of freedom provides effective colloid–colloid interactions, and if these match those of an atomic system, the *equilibrium phase* behavior is the same [3, 4].

This equivalence need not hold for the description of time-dependent features, or when the systems are driven far from equilibrium. However, the long-time dynamics close to the glass transition provides a notable exception: here, although the theoretical description of the microscopic dynamics of the systems differs (Newtonian for metallic melts, Brownian for colloidal particles), the near-equilibrium structural relaxation is equivalent due to

Dedicated to Matthias Ballauff on occasion of his retirement

✉ Thomas Voigtmann
thomas.voigtmann@dlr.de

Miriam Siebenbürger
msiebenbuerger@lsu.edu

[1] Institut für Materialphysik im Weltraum, Deutsches Zentrum für Luft- und Raumfahrt (DLR) e.V., Linder Höhe, 51170, Köln, Germany

[2] Center for Advanced Microstructures and Devices, Lousiana State University, Baton Rouge, LA, 70803, USA

[3] Universität Konstanz, 78457, Konstanz, Germany

[4] Heinrich Heine University, Condensed Matter Physics Laboratory, Universitätsstraße 1, 40225 Düsseldorf, Germany

[5] Universität Konstanz, 78457, Konstanz, Germany

[6] Universität Göttingen, Friedrich-Hund-Platz 1, 37077, Göttingen, Germany

[7] Department of Chemistry "Ugo Schiff" and CSGI, University of Florence, Sesto Fiorentino, Florence, I-50019, Italy

the dominance of slow relaxation processes that are driven by local density fluctuations [5, 6]. This equivalence is widely accepted and well tested [6–10]; it arises because the structural relaxation time τ of the system is well-separated from the much shorter time scale τ_0 that characterizes the (vibrational or diffusive) short-time motion of the particles. The mode-coupling theory of the glass transition (MCT) makes this observation rigorous [5, 11] and predicts a critical temperature T_c (or, for colloidal suspensions of hard spheres, a critical packing fraction φ_c) that separates the high-temperature (low-density) liquid-like relaxation behavior from a regime of low-temperature (high-density) solid-like relaxation. Yet, while MCT implies that the glass-transition point itself is unchanged by the kinetic parameters of a system, the dynamics in its vicinity might show different dependence on, for example, mobility ratios in mixtures depending on whether one is on the liquid side or the glass side of the MCT transition [12]. It is worth stressing here that, since the glass transition is a *kinetic* phenomenon, the equivalence of dynamical features is not trivial. As a counter-example, consider the Lorentz model of a single tracer moving in a random heterogeneous medium. Based on the different mechanism by which Newtonian and Brownian particles probe the narrow channels between obstacles, different dynamical critical exponents are predicted, in agreement with recent simulations [13].

An analogy between yielding in colloidal glasses and metallic glasses has often been invoked, but remained rather qualitative. The unique mechanical properties of bulk metallic glasses (BMG) make this a technologically promising route to study, even though the deformation-behavior map of such glasses has different regimes where different analogies may be fruitful [14]. A key point to note here is that metallic, as most small-molecular, glasses are usually studied close to the empirical calorimetric glass-transition temperature T_g, significantly below the mode-coupling transition temperature T_c. At T_g, the viscosity of the system is usually some ten orders of magnitude more separated from the high-temperature one, when compared with the viscosity around T_c. Even though some aspects of the *non-equilibrium* nonlinear rheology appear similar [15, 16], and both in metallic glasses and in deeply quenched colloidal glasses, similar local shear-transformation zones (STZ) could be identified as microscopic signatures of yielding [17–19], there are important differences. Colloidal dispersions typically deform plastically over a broad range of strains; metallic alloys deform plastically on the atomic scale, which determines their casting properties, but they typically fail as brittle solids by shear banding [20].

Here, we discuss aspects of the rheology of both some exemplary metallic alloys and of prototypical colloidal hard-sphere-like dispersions, to demonstrate regimes of macroscopic linear and nonlinear response where the behavior of the two system classes can be mapped qualitatively and quantitatively. The mapping is based on the notion that the typical scale for stresses in a material is set by the thermal energy-density scale k_BT/R^3, where R is the typical size of a constituent particle. The change from $R \sim 1\,\mathrm{nm}$ typical of metallic alloys to $R \sim 1\,\mu\mathrm{m}$ typical of colloidal matter includes a change of nine orders of magnitude in the stresses. Although this observation is the well-recognized core of distinguishing "hard" from "soft" matter [1], it has remained rather qualitative so far. In our contribution, we aim to demonstrate how far into the quantitative this analogy can be pushed.

We combine experimental data on colloidal suspensions and on metallic melts with molecular dynamics (MD) and Brownian dynamics (BD) simulations, in order to demonstrate the qualitative and quantitative aspects of mapping hard- and soft-matter rheology also for those cases (focusing on microscopically resolved quantities) where metallic-alloy data is not readily available. The qualitative features of the data are rationalized by MCT and simple models based on it.

We combine colloidal data on different approximations to the hard-sphere model system: one is based on core-shell microgels where a thermosensitive crosslinked network of poly(N-isopropylacrylamide) (PNiPAM) is affixed onto a poly(styrene) (PS) core. These PS-PNiPAM particles were established as excellent hard-sphere model systems for the study of relaxation phenomena close to the colloidal glass transition in particular by Matthias Ballauff and coworkers [21–25]. Their thermosensitive shell makes it possible to fine-tune the hard-sphere packing fraction by changes in sample temperature. The other system is one of PMMA particles representing a well-established colloidal hard-sphere model. Experiments on this system allow resolving the microstructure under flow, by combining developments in standard rheometry with microscopy [18, 19, 26–28], and with algorithms to determine with high accuracy the positions of particles from confocal-microscopy images [29].

Linear rheology

We begin by reviewing the most basic information on the linear rheology of glass-forming fluids, i.e., the change in shear viscosity as the glass transition is approached by either lowering the temperature or increasing the packing fraction.

For a mixture of hard spheres, the total packing fraction φ is defined by $\varphi = (\pi/6)n\sum_\alpha x_\alpha d_\alpha^3$ where n is the number density of the particles and d_α is the diameter of the particles of the species labeled by α, whose number concentration is x_α. An effective packing fraction φ is

often used as a proxy to estimate the slowing down of structural relaxation in metallic melts [30], assuming that in the liquid regime, a dominant contribution to the slow relaxation comes from excluded volume between the atomic constituents. One typically obtains in sluggish metallic melts an effective packing fraction of $\varphi \approx 0.55$. This compares to the reference value $\varphi_c \approx 0.58$ obtained for hard-sphere colloidal suspensions [31] at their MCT transition (and hence corresponding to T_c). Since the density of the melt typically increases with decreasing temperature, one indeed finds that higher packing fractions give rise to higher viscosities. However, on this level, the hard-sphere analogy of metallic melts is rather qualitative (and needs to be—it is well known that different melts display different chemical interaction effects, different "fragilities" close to the glass transition, etc.)

For the calculation of φ, one needs accurate density data, and a set of empirical atomic radii. The choice of the latter is crucial because φ depends cubically on the d_α. One choice was proposed by Miracle [32], but these radii consistently give values of $\varphi \approx 0.64$, close to the accepted random-close-packing limit of (monodisperse) hard spheres. In other words, this choice of radii reiterates the observation that dates back to Bernal [33], that the liquid structure bears resemblance to the disordered close-packed arrangement of spheres. Another common choice for the effective atomic sizes is due to Pauling [34]. These values are related to the positions of the first maximum in the radial distribution function and hence already absorb some chemical-environment effects mediated through electronic degrees of freedom. We will adopt this choice in the following.

Metallic melts where both accurate viscosity data (spanning a large viscosity range) and density data are available, are not abundant in the literature. We focus here on Zr-based melts; experimental data are available for the binary $Zr_{64}Ni_{36}$ [35] and the five-component bulk-metallic glass former Vitreloy Vit106a ($Zr_{58.5}Cu_{15.6}Ni_{12.8}Al_{10.3}Nb_{2.8}$ [37]), measured using electrostatic and electromagnetic levitation techniques. We complement these data by those from molecular-dynamics simulations of Zr-Ni-Al melts whose MD interaction potentials have been carefully matched with structural and dynamical experimental data [36].

The data span just above one to three decades in slowing down in viscosity for experiment and simulation. They concur with a similar increase in the structural relaxation time τ. In this range, the effective packing fractions obtained using Pauling's empirical radii range between $\varphi \approx 0.53$ and $\varphi \approx 0.57$ (inset of Fig. 1); the packing-fraction-dependent viscosity data of three of the systems almost collapse, while the system with the highest Al content deviates significantly. It has been discussed in the literature that the addition of Al to metallic melts causes strong chemical interaction effects that become particularly pronounced above a certain Al concentration (see, e.g., Refs. [39–42]), so that this deviation can be rationalized.

On the other hand, the quantitative agreement with the hard-sphere model is not convincing. To see this, we include in the analysis data collected from various colloidal hard-sphere models (collected by Russel, Wagner, and Mewis [38], see there for original references). This data shows that at a nominal packing fraction above $\varphi = 0.5$, the viscosity is already at least two orders of magnitude slower than the low-density reference, and that it increases by

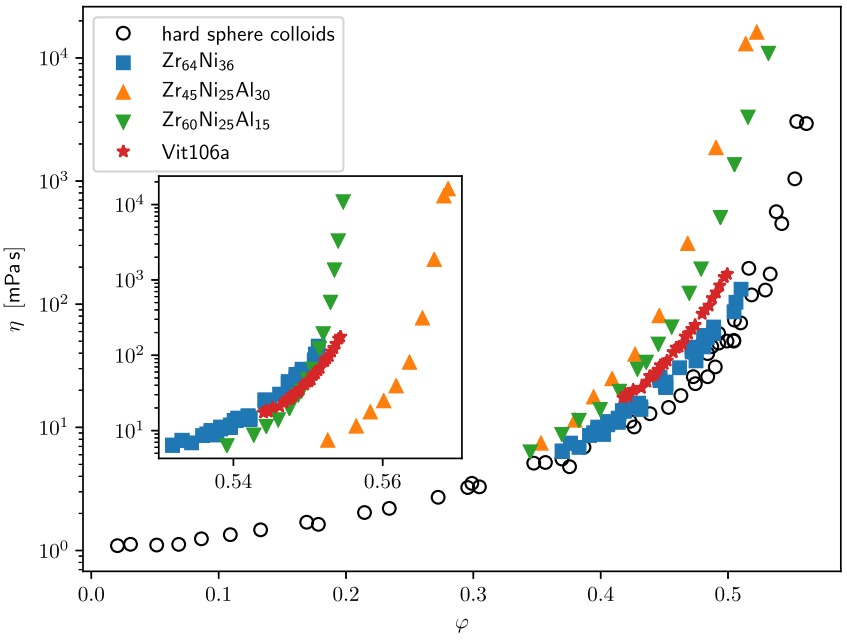

Fig. 1 Viscosity of selected metallic melts (filled symbols as labeled; $Zr_{64}Ni_{36}$ from experiment [35]; $Zr_{75-x}Ni_{25}Al_x$ from molecular dynamics simulations [36]; Vit106a, $Zr_{58.5}Cu_{15.6}Ni_{12.8}Al_{10.3}Nb_{2.8}$ from experiment [37]) as a function of empirical packing fraction φ, compared with the viscosity obtained from various hard-sphere-like colloidal suspensions (collected in and taken from Ref. [38]; assuming a solvent viscosity of 1 mPa s). Main panel: using empirical diameters $d_{\mathrm{eff},\alpha} = d_\alpha (T/T_0)^{-n}$, with $n = 0.2$ and $T_0 = 950$ K and d_α from Pauling [34]; inset: using d_α without temperature correction

three orders of magnitude in a window of packing fractions of width $\Delta\varphi \approx 0.15$. On the contrary, the effective mapping of metallic-alloy data suggests the same increase in viscosity to occur in the much more narrow window of $\Delta\varphi \approx 0.02$.

One ad hoc way to account for this difference is provided by admitting the effective diameter of the spheres to vary as a power law in temperature, $d_{\mathrm{eff},\alpha} = d_\alpha (T/T_0)^{-n}$, as would be expected for effectively soft-sphere interactions. Such softness in the interatomic repulsion has a strong impact on the fragility of supercooled metallic melts and through the shear modulus also on the viscosity [43]. Empirically, the exponent n quantifies the softness of interactions and T_0 is a reference temperature for the choice of d_α. One thus obtains a corrected effective packing fraction (main panel of Fig. 1). Without wanting to emphasize the "correct" choice of T_0 and n, the comparison of this rescaled data with the colloidal reference shows much better agreement.

Already in the hard-sphere model, one expects the value of φ where a sharp increase in viscosity is observed (attributed as being due to a close-by glass transition) to vary with composition and size ratio of a mixture. In colloidal suspensions and soft-matter systems, most studies focus on the regime of very size-disparate mixtures (see, e.g., Refs. [44–54] for studies of glassy dynamics and Refs. [55–57] for the linear and nonlinear rheology). The size polydispersity inherent in colloidal suspensions also shifts φ_c, but less dramatically so. For typical metallic-alloy atoms, the relevant size ratios are in the range of 0.8 to 1.0, and for binary mixtures of such size ratios, MCT calculations predict that the glass-transition point shifts to slightly lower packing fraction [52]. This effect has been found in molecular-dynamics simulations [58] and is not in disagreement with the trend observed in Fig. 1 for the metallic-alloy data.

Note that to emphasize the analogy between atomistic and colloidal rheology, one should further express the viscosity in scaled units. The typical time scale that is needed in order to non-dimensionalize a viscosity can be expressed in terms of the short-time Brownian diffusion scale for a colloidal system, $\tau_0 = R^2/D_0 = 6\pi\eta_s R^3/k_B T$ with the solvent viscosity η_s, or the thermal-velocity time scale for an atomistic system, $\tau_0 = R/\sqrt{k_B T/m}$. Hence, a typical viscosity scale is set by the solvent viscosity for a colloidal system, and by $\sqrt{k_B T m}/R^2$ for a molecular system. We have not included this conversion in Fig. 1 because the choice of τ_0 for the metallic mixtures is not evident; also the conversion would need to account for hydrodynamic-interaction effects in the colloidal system. Note that for Zr atoms, which make up the majority of atoms in the metallic alloys in our comparison, using $m_{\mathrm{Zr}} = 91.224\,\mathrm{u}$ where $\mathrm{u} \approx 1.66 \times 10^{-27}\,\mathrm{kg}$ is the atomic mass unit, and $R_{\mathrm{Zr}} \approx 1.45\,\text{Å}$, one gets $\sqrt{k_B T m}/R^2 = \mathcal{O}(10^{-3}\,\mathrm{Pa\,s})$, so that mPa s is indeed the natural viscosity scale for both system types.

Startup flow

An important rheological characterization of materials are the stress–strain relations. In the corresponding "start-up" experiment, one applies, starting at time $t = 0$, and a deformation at a fixed rate $\dot\gamma$, and records the resulting macroscopic stress σ as a function of accumulated strain $\gamma = \dot\gamma t$.

Startup curves for glasses typically display three regimes as a function of strain γ (see Fig. 2): a linear increase $\sigma \simeq G_{\mathrm{eff}}\gamma$ indicating the initially nearly elastic response of the material at low strains with an effective shear modulus G_{eff}, and a strain-independent plateau of the stress at large γ (corresponding to large times), where σ is a function of $\dot\gamma$ rather than γ and signals that the material responds as a viscous fluid. At intermediate strains, the σ-versus-γ curves obtained for large enough strain rate display a characteristic maximum, termed the stress overshoot. This stress overshoot usually occurs at strains around $\gamma \approx 0.1$, which can be termed a yield strain. Its numerical value is often attributed to the Lindemann criterion of melting [61], and it provides a unified view on temperature-induced and strain-driven transitions in metallic glasses [62]. One can interpret the stress overshoot as the breaking of cages due to deformation forces. This process sets in when the yield stress of the material is reached, but the initial breaking of cages requires a stress that is somewhat larger than that sustained once the microscopic structure of the materials adjusts to flow. Cages hence can be said to store some amount of elastic energy [63, 64].

Based on the hard-sphere analogy, it is suggestive to compare the stress–strain curves of colloidal hard-sphere dispersions, and of bulk metallic glasses. Some caveats are in order when doing so: first, colloidal particles are embedded in a solvent, and thus the typical deformation works at constant volume, while it is performed at constant pressure in metallic systems. Furthermore, while for colloidal suspensions it is convenient to apply simple shear stress, experiments on metallic glasses usually work in tension or compression. In principle, the deformation and in particular the yielding behavior will depend on the geometry of the stresses and strains. The question of which deformation modes are most effective in yielding an amorphous material leads to various empirical yield criteria. Calculations within the mode-coupling theory of colloidal rheology [65] recover, up to small deviations that are understood as arising from normal-stress differences, the so-called von Mises' criterion which asserts that yielding is predominantly driven by the total elastic energy deposited

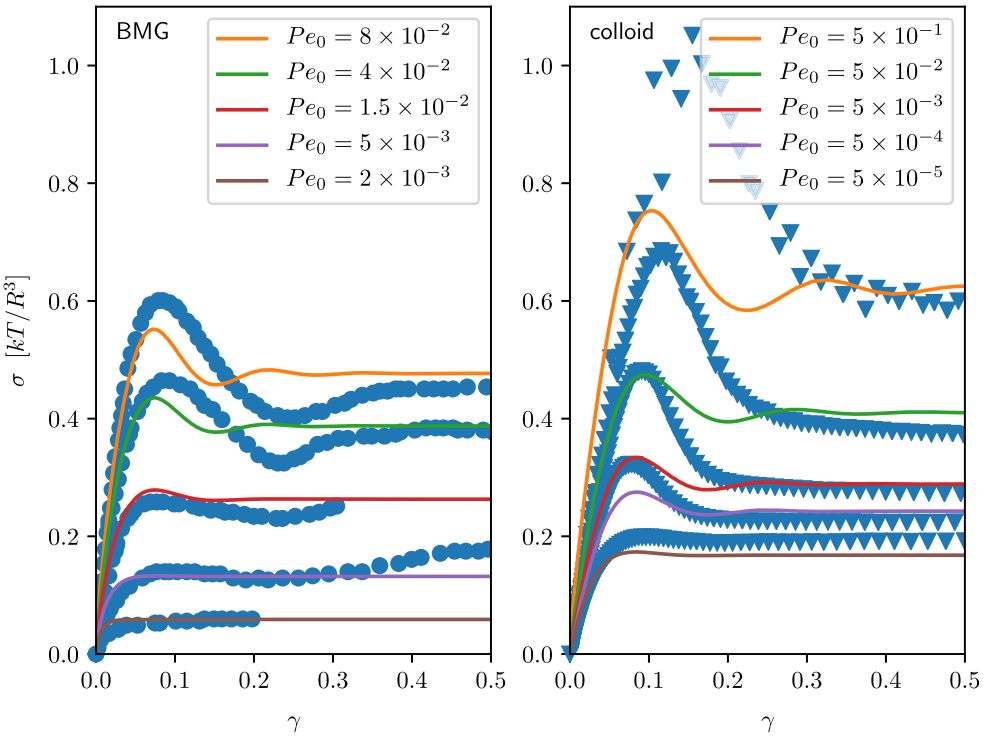

Fig. 2 Stress σ versus strain γ for different deformation rates given as Péclet numbers Pe_0. Left: for a bulk metallic glass (Vitreloy 1, $Zr_{41.2}Be_{22.5}Ti_{13.8}Cu_{12.5}Ni_{10}$, $T = 613$ K, from Ref. [59]; strain rate rescaled by $\sqrt{3}$ to account for the deformation geometry, see text). Right: for colloidal hard spheres (PS-PNiPAM, $\phi \approx 0.60$, from Ref. [60]). Lines are fits using a sheared-hard-sphere model of MCT in isotropic approximation (see text for details), rescaled by 0.75 and 0.32 for the BMG and the colloidal sample, respectively, and using strain-scale parameters of $\gamma_c = 0.3$ and $\gamma_c' = 0.12$ (BMG; left), and $\gamma_c = 0.3, 0.2, 0.2, 0.2, 0.1$ and $\gamma_c' = 0.18, 0.16, 0.14, 0.14, 0.14$ (colloid for increasing Pe_0; right), see Appendix A for details

in the material (in either deformation geometry). Under this assumption, it is plausible to compare stress–strain curves obtained under different deformation geometries, once one relates the effective strain rates by a geometrical factor.

In particular, an arbitrary homogeneous deformation is characterized by the strain-rate tensor $\boldsymbol{\kappa}$, defined as $\kappa_{ij} = \partial_j v_i$ where i, j are the Cartesian components and $\mathbf{v}$ is the homogeneous velocity field of the deformation map. Then, a scalar local strain rate can be defined as the second invariant of the symmetrized strain-rate tensor, $\boldsymbol{D} = \boldsymbol{\kappa} + \boldsymbol{\kappa}^T$, via $\dot{\gamma} = II_{\boldsymbol{D}} = \sqrt{(1/2)tr\boldsymbol{D} \cdot \boldsymbol{D}}$ for a deformation that is incompressible, i.e., where $tr\boldsymbol{D} = 0$. For simple shear, $\kappa_{xy} = \dot{\gamma}$ is the only non-zero element of the strain-rate tensor. Uniaxial deformation corresponds to $\kappa_{xx} = \dot{\gamma}_{\text{uniax}}$, and $\kappa_{yy} = \kappa_{zz} = -\dot{\gamma}_{\text{uniax}}/2$, so that $II_{\boldsymbol{D}} = \sqrt{3}\dot{\gamma}_{\text{uniax}}$ (cf. also Ref. [66]).

In Fig. 2. we compare the stress–strain curves of a bulk metallic glass (Vitreloy 1; $Zr_{41.2}Be_{22.5}Ti_{13.8}Cu_{12.5}Ni_{10}$) obtained under uniaxial extension (left panel, from Ref. [59]) with those of a typical PS-PNiPAM hard-sphere suspension under simple shear [60] (right panel). Data are shown for various deformation rates $\dot{\gamma}$, converted into dimensionless Péclet numbers $Pe_0 = \dot{\gamma}\tau_0$ using the time-scale of short-time motion τ_0. The strain rates for the BMG were related to that of simple shear by a geometric factor, $\dot{\gamma} = \sqrt{3}\dot{\gamma}_{\text{uniax}}$, as discussed above.

An important conclusion from the comparison is that in both systems, thermal energy sets the natural stress scale: after rescaling the stresses with k_BT/R^3, where R is a typical atomic or colloidal radius (using $R = 1.58$ A in Fig. 2 based on the Pauling radius for Zr as the majority species and corrected for temperature as above), both the startup stresses for the metallic and the colloidal glass are of order unity for typical flow rates, and comparable to each other provided that the deformation rates (as expressed in dimensionless Péclet numbers) are also comparable. The quantitative comparability holds, even though the BMG data is obtained at $T = 613$ K, close to and in fact below the calorimetric glass transition temperature, $T_g \approx 623$ K, while the colloidal data is obtained at a packing fraction $\varphi \approx 0.60$ close to the location of the MCT transition point in this experimental system. In essence, the comparison thus emphasizes that for the macroscopic stress–strain curves not too deep in the glassy state and at sufficiently low shear rates, the Péclet number is the only relevant dimensionless parameter that determines the shear-induced structural relaxation. Note that for deformation deep in the glassy state (which is particularly relevant not only for BMG at room temperature, but also for colloids closer to jamming), other deformation modes might become relevant; to address the spatially heterogeneous plastic deformations (shear bands, etc.) of the amorphous solid is beyond the scope of this paper.

The initial, nearly linear increase of the σ-versus-γ curves allows estimation of the Maxwell plateau modulus of the system. Again, for both systems, the values are comparable once expressed in appropriate thermal-energy units: from the BMG data, $G_\infty \approx 14$ GPa $\approx 14\, k_BT/R^3$,

while for the colloid data, $G_\infty \approx 42\,\mathrm{Pa} \approx 7.7\,k_BT/R^3$ (where $R = 90\,\mathrm{nm}$ is the average radius of the colloids). Similar results are also obtained using startup rheology of PMMA hard-sphere-like colloidal suspensions of sizes $R = 150\,\mathrm{nm}$ and $R = 780\,\mathrm{nm}$, where after rescaling data for comparable Péclet numbers by k_BT/R^3, the stationary stresses [67] and the stress–strain curves [68] coincide.

Lines in Fig. 2 demonstrate results from MCT obtained for the hard-sphere system (using the Percus-Yevick approximation for the static structure factor, and an isotropic approximation for the MCT vertices in the integration-through transient, ITT, formalism). Details of the calculation can be found in Appendix A. In the calculation, state points close to the MCT glass transition were chosen, such that the structural relaxation times τ match the ones estimated for the experiments in dimensionless units.

ITT-MCT captures well the overall trend of the stress–strain curves and their dependence on Pe_0. However, the stress overshoots are systematically underestimated in the isotropic ITT-MCT approximation. This is likely a combination of several factors: beyond the effect of approximations inherent in the isotropically averaged ITT-MCT model, the theory also refers to startup flow from a well-equilibrated sample. In the experiment, it is known that the magnitude of the stress overshoot depends sensitively on the sample preparation and its age (with older samples typically displaying larger stress overshoots) [60, 69, 70]. Also, shape and strength of the stress overshoot depend sensitively on the microscopic details of the interaction, and here, deviations from idealized hard-sphere behavior are most likely to be prominent [71]. In this regard, PMMA suspensions were argued to be closer to ideal hard-sphere behavior than the PS-PNiPAM particles; indeed, the former display weaker overshoots [72]. For a comparison between PMMA startup curves and MCT, see also Ref. [73].

Note that although the common terminology implies a single maximum in the stress–strain curve, there is no inherent reason that excludes a more general damped-oscillatory crossover from the linear-elastic to the plastic-flow regime. Indeed, such oscillations are seen in both the theory and the BMG data; they have also been observed at high Pe in colloidal suspensions [74]. BMG tend to break after applying strains much larger than the yield strain, so that this regime is difficult to access there. Within ITT-MCT, the oscillations arise because of a slight mismatch in the relaxation times of the relevant density fluctuations and the affine decorrelation of the coupling between these density fluctuations and the overall stresses. As detailed in Appendix A, in the theory, this is tuned by strain-scale factors γ_c and γ_c', whose empirical values are given in the caption of Fig. 2; they were chosen such that the ITT-MCT results roughly match the position and strength of the experimentally observed stress overshoots (as far as possible within the simplified MCT model). In principle, the stress overshoot is thus rationalized as a competition between reversible affine deformation (as expressed through shear advection) and the irreversible relaxation dynamics, i.e., the competition between elastic storage and dissipative loss of strain energy.

There is a direct link between the anisotropy of the microscopic structure and the macroscopic stresses in a sheared system. We note in passing that also for the quiescent systems, the statistical information on the microstructure, as expressed through the static structure factor $S(q)$ and the related radial distribution function $g(r)$, emphasizes the qualitative similarities between the metallic and the colloidal systems. This becomes clearer if one focuses on binary metallic alloys where isotope-substitution scattering experiments allow the determination of the partial static structure factors that can then be compared with predictions of the hard-sphere model. For the example of Zr-Ni melts [75, 76], this also demonstrates the extent of chemical short-range order effects on the dynamics.

A direct way to quantify the microstructural changes under deformation is through the change of the radial distribution function $\delta g(\mathbf{r}) = g(\mathbf{r};\dot\gamma) - g_{\mathrm{eq}}(r)$, where $g(\mathbf{r};\dot\gamma)$ is the (anisotropic) stationary distribution function under shear, and $g_{\mathrm{eq}}(r)$ the (isotropic) one of the quiescent system. Simulations readily give access to this quantity. To demonstrate the qualitative features, we have extracted this quantity from molecular-dynamics (MD) simulations of a model of liquid Ni and from Brownian dynamics (BD) simulations of a 2D hard-disk system (see Appendix C for details of the simulations). In both systems, qualitatively similar distortion patterns are seen (Fig. 3), despite the difference in interaction potential (soft versus hard) and dimensionality. One notes in particular a quadrupolar distortion that is expected on grounds of the rotational symmetry imposed under simple shear: along a compression axis (at $\theta \approx 135°$ w.r.t. the flow direction), particles are pushed on average closer together than in the quiescent state, and along an extension axis ($\theta \approx 45°$), they move further apart. For the Ni system, this implies that $\delta g(\mathbf{r})$ is enhanced close to the nearest-neighbor peak of $g_{\mathrm{eq}}(r)$ along the compression axis, and suppressed along the extension axis. For increasing radial distance r, this pattern of enhancement and suppression alternates and indicates that the dominant effect indeed is a quadrupolar distortion of the local atomic distances. The same effect is seen in the hard-sphere simulation, although here, the signal in $\delta g(\mathbf{r})$ is much sharper. This is due to the fact that hard spheres can, other than the soft Ni atoms, not be pushed closer together than their hard-sphere interaction diameter, where $g_{\mathrm{eq}}(r)$ already has a very pronounced maximum. (Also, in the hard-sphere simulation, a binary mixture was considered in order

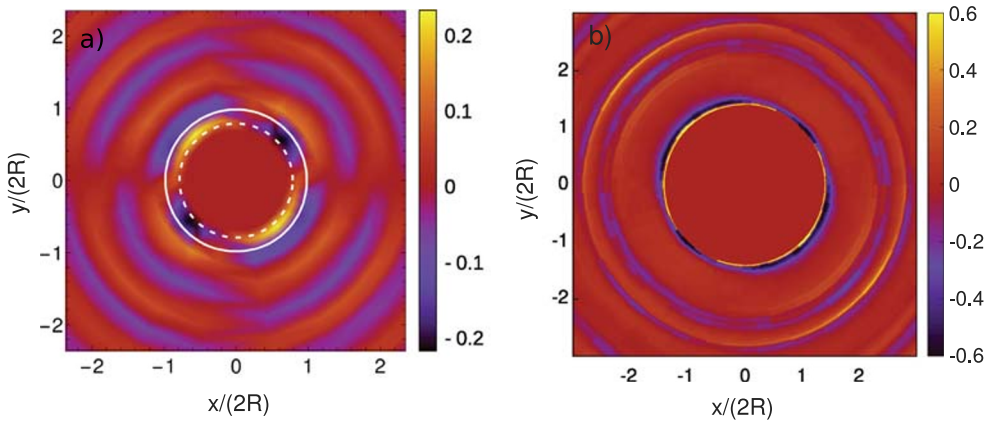

Fig. 3 Distortion of the radial distribution function, $\delta g(\mathbf{r}) = g(\mathbf{r};\dot{\gamma}) - g_{\mathrm{eq}}(r)$, under shear flow of rate $\dot{\gamma}$, displayed in the shear–shear-gradient plane (x: direction of flow, y: direction of gradient). (a) from molecular-dynamics (MD) simulations of a model of Ni; (b) from Brownian dynamics (BD) simulations of a binary hard-sphere system with size ratio $\delta = 0.8$. Dashed and solid white circles are guides to the eye to emphasize cuts of constant r where $l = 2$ and $l = 4$ deformations can be seen (two minima interspersed by two maxima, respectively four separated minima)

to avoid crystallization, which leads to additional rings in the appearance of Fig. 3b compared with the monodisperse Ni system.)

While the quadrupolar distortion agrees with the expectation from continuum mechanics (where one would argue that a symmetric second-rank tensor such as the stress tensor can be decomposed into multipole terms including the monopole and a quadrupole), a closer inspection of $\delta g(\mathbf{r})$ reveals a growing amount of higher-order distortion [77]. We discuss this point in the following, for the spherical-harmonic projections of $\delta g(\mathbf{r})$ and cuts along constant radial distance r.

The leading non-trivial spherical-harmonic projections of $\delta g(\mathbf{r})$ confirm that on distances corresponding to nearest-neighbor shells around particles, different local deformation modes prevail (Fig. 4), both in the MD simulation representative of the metallic system, and in experiment on the colloidal hard-sphere-like suspension. To obtain the latter data, we have developed a high-precision setup that allows confocal-microscopy imaging of a flowing colloidal suspension combined with accurate localization of the particles through image analysis. Details of the technique as well as our convention of the projections $\delta g_{lm}(r)$ are presented in Appendix D.

The quadrupolar term $\delta g_{22}(r)$ (solid lines) indicates the shift of particles inward along the compression axis, and outward along the extension axis; there results an oscillatory signal in $\delta g_{22}(r)$ with a zero around the equilibrium nearest-neighbor distance $r \approx 2R$. In fact, the inward shift of particles is stronger than the outward push, as is revealed

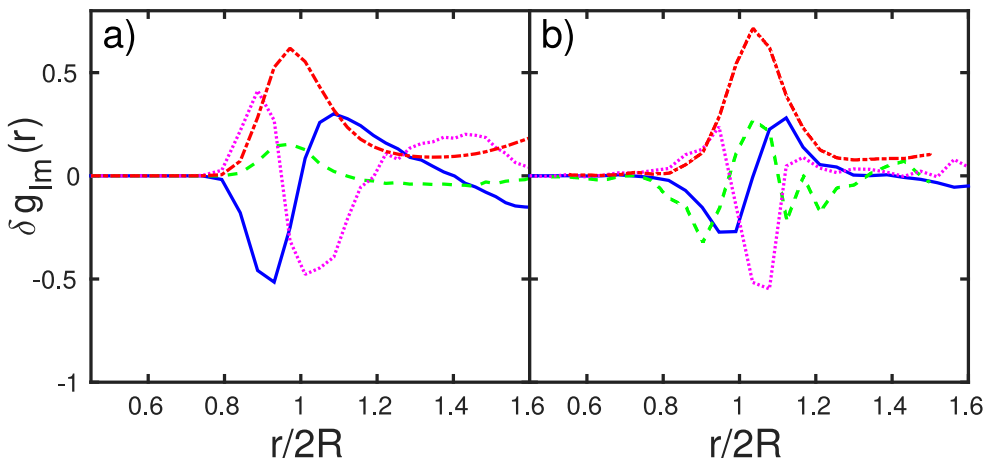

Fig. 4 Spherical-harmonics projections of the distorted radial distribution function, $\delta g_{lm}(r)$, as a function of radial distance in units of a typical particle size. Dotted line (magenta): isotroptic change $\delta g_{00}(r)$; solid line (blue): quadrupolar distortion $\delta g_{22}(r)$; dashed line (green): hexadecupolar distortion $\delta g_{44}(r)$. The quiescent radial distribution function is shown as $g_{\mathrm{eq}}(r)/5$ (red dashed line) for comparison. **a** From MD simulations of liquid Ni. **b** From confocal microscopy data of a PMMA hard-sphere colloidal suspension

by an overall isotropic contribution $\delta g_{00}(r)$ that has a maximum slightly inward of $r = 2R$, and a minimum at distances somewhat larger than the quiescent nearest-neighbor distance (dotted lines in Fig. 4). The isotropic contribution indicates that under shear, there is a flow-induced enhancement of the pressure. Such an increase in pressure has been linked to shear banding [78, 79] which in turn is sometimes linked to the appearance of stress overshoots [80, 81]. Note on the contrary that in the simulations it has been verified that the flow remains homogeneous for all the states that are considered here.

At the distance of the quiescent nearest-neighbor shell, both the isotropic and the quadrupolar distortions nearly vanish. There remains however a hexadecupolar term, $\delta g_{44}(r)$ (dashed lines), as pointed out previously in the context of MCT [77]. It has been attributed to specific non-affine rearrangements of particles under the constant breaking of cages due to shear. It is remarkable that this signal, unexpected from continuum symmetry, can indeed also be identified in the confocal-microscopy data of a colloidal suspension, as demonstrated in Fig. 4b.

The interpretation that the hexadecupolar distortion signals constant non-affine local rearrangements that are indicative of the fully yielded system [77] is consistent with the expectation that for small strains, only a quadrupolar distortion should prevail [63, 64, 82]. This is indeed the case, as seen by a comparison of the different angular dependence of $g(\mathbf{r}) \equiv g(r, \theta)$ in the flow–flow-gradient plane, at constant $r \approx 2R$ (Fig. 5). For small strains that are still in the linear-elastic regime, $\delta g(r, \theta)$ is well described by a quadrupolar angle dependence $\propto \sin 2\theta$, which is also linear in the strain as expected for reversible deformations. Both in the MD simulations of liquid Ni and in the colloidal experiment do we observe that for strains larger than the yield strain, $\gamma \gtrsim 0.1$, the same angular dependence is best described by the $l = 4$ form $\propto (\sin 2\theta)^2$ (bottom set of curves in Fig. 5) that is quadratic in the strain, as indicative of irreversible deformations.

The cross-over from quadrupolar to hexadecupolar symmetry in $\delta g(2R, \theta)$ is qualitatively explained by numerical solutions of the full ITT-MCT equations combined with an expression for the distorted structure factor [83]. We compare (inset of Fig. 5) with the ITT-MCT prediction of a two-dimensional hard-disk system; this choice allows to significantly reduce the numerical complexity of the MCT calculation and also serves to demonstrate the generality of the result: The same evolution of $\delta g(\theta)$ is seen as in the simulations and experiments performed on 3D, slightly soft and polydisperse particles. As a result of the strict hard-sphere approximation, the distortion of $g(\mathbf{r})$ directly at contact, $r = 2R$, is however much more pronounced, as anticipated from the discussion of Fig. 3. The ITT-MCT curve highlights that the local minimal in $\delta g(\theta)$ are at angles slightly different from 45° an 135° and closer to 35.3° and 144.7° respectively. To understand this, recall that after a rotation of the coordinate system by $\pi/2$, these locations correspond to the "magic angle" $\theta_c = 54.7°$ given by the zero of the second-order Legendre polynomial. Coincidentally, in continuum elasticity these are the directions expected for shear bands forming in the locations where normal stresses vanish, e.g., in the deformation of rubber [84, 85].

It is interesting to note that the appearance of $l = 4$ distortions, which by continuum symmetry cannot directly enter the stress tensor but do so indirectly through the effect of the associated particle motion also on the $l = 2$ mode, might be the signal of local particle rearrangements such as

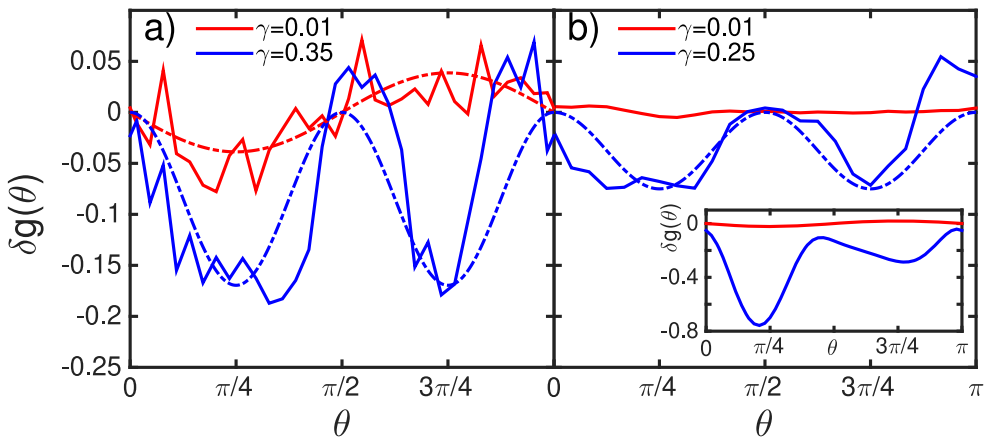

Fig. 5 Angular dependence of $g(\mathbf{r})$ at fixed radial distance $r \approx 2R$, as a function of the angle to the shear-flow direction, θ, for two strains γ after startup flow before ($\gamma = 0.01$: top curves) and after ($\gamma > 0.1$: bottom curves) the yield strain. Dash-dotted lines are fits using a quadrupole signal $\sin 2\theta$ (top) and a hexadecupolar signal $(\sin 2\theta)^2$ (bottom). **a** From MD simulation of liquid Ni. **b** From confocal microscopy of a PMMA hard-sphere colloidal suspension ($r = 2.1R$). Inset: Results from mode-coupling theory (ITT-MCT) for a 2D hard-disk system

the ones triggering STZ, ultimately causing yielding as seen from a microscopic point of view. In similar vein, they could be linked to the T1 events in emulsions and foams [86, 87] (systems where also stress overshoots are seen [88]): such individual plastic events release stress locally and hence are thought ultimately responsible for yielding, yet they are not easily linked to the macroscopic stress [89, 90].

Shear-history effects

A major effect of slow structural relaxation on the rheology of viscoelastic fluids and amorphous solids is the appearance of flow-history effects. Changes in the flow conditions at previous times $t' < t$ influence the response at time t for the large time interval up to $t-t' \sim \tau$. In principle, in the ideal glassy state, this interval extends arbitrarily far back in time. This causes for example frozen-in stresses in a sample that has been flowing at $t < 0$ and whose flow is stopped at $t = 0$. In the glass, in principle, a stress $\sigma_\infty \neq 0$ is observed even as $t \to \infty$, and this stress depends on the infinitely past flow conditions. Again, colloidal model suspensions provide clean model systems in which to study these effects [67]. With their help, also the response in amorphous metallic materials can be understood, based on the hard-sphere analogy.

A related effect was first described by Bauschinger [91] in the case of steel samples: in general, the elastic response of a material depends on the way it has been pre-strained. In crystalline materials, pre-strain can induce obvious micro-structural changes such as the healing or creation of lattice defects and grain boundaries. But also in amorphous materials, there are (more subtle) strain-dependent changes in the microstructure that will affect the subsequent stresses. A slightly formalized version of the measurement was proposed in the context of glasses, aiming to address the so-called Bauschinger effect [92, 93]: the initial sample is first sheared as in startup flow for a certain time, until a pre-strain γ_w has been reached. After the corresponding "waiting time" $t_w = \gamma_w/\dot\gamma$, the shear is reversed, keeping the rate constant, i.e., $\dot\gamma(t > t_w) = -\dot\gamma(t < t_w)$. After the stress has reached zero for some $t_0 \gtrsim t_w$, a reversed stress–strain curve is recorded.

The Bauschinger effect manifests itself by an altered response: the typical stress-overshoot, whose maximum indicates a certain static yield strength of the material, is strongly reduced after large pre-strains γ_w. Experiments on PS-PNiPAM suspensions demonstrate this (Fig. 6): for $\gamma_w \lesssim 14.4\%$, some remnant overshoot is still seen, but upon flow reversal after a pre-strain of order unity, a stress–strain curve essentially without overshoot is observed. This finding agrees with MD simulations of a molecular glass former [93]. Within ITT-MCT, this is explained [93] as a balance of two contributions to the generalized Green-Kubo integral that determines $\sigma(t)$ from all $t' < t$: a positive overshoot arising from $t' \sim (t_w - \gamma_c/|\dot\gamma|) < t_w$ and a negative one arising from $t' \sim (t_w + \gamma_c/|\dot\gamma|)$ that cancel each other if both contributions are well within the stationary regime of the flow. Indeed, as γ_w is increased from zero, the stress overshoot starts to vanish as soon as $\gamma_w \gtrsim \gamma_c$.

ITT-MCT describes the reduction of the stress overshoot qualitatively, and to emphasize the cancellation mechanism

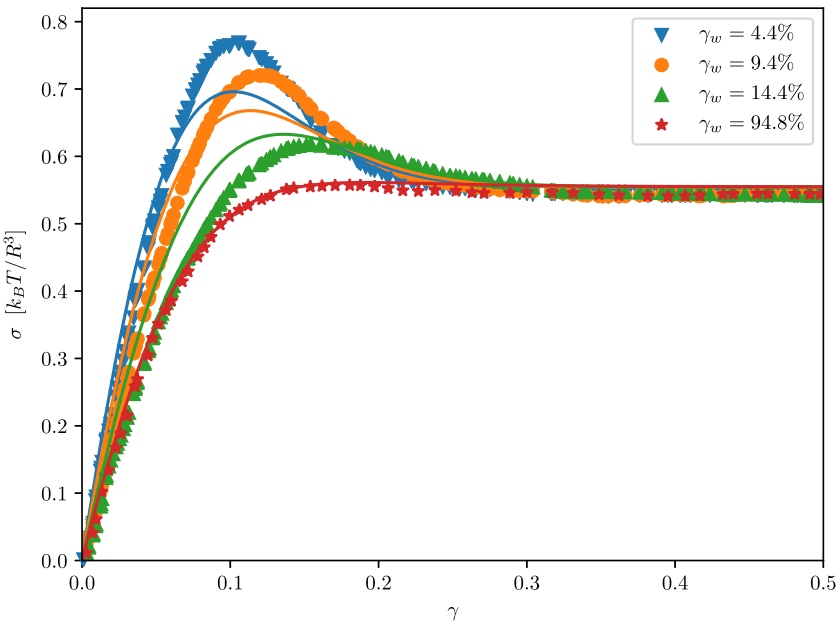

Fig. 6 Symbols: Stress–strain curves of a colloidal hard-sphere-like suspension (PS-PNiPAM particles, $R \approx 90$ nm) after different amounts of pre-strain γ_w in the opposite direction, at a shear rate of $\dot\gamma = 5 \times 10^{-4}\,\mathrm{s}^{-1}$. Lines: Results from a generalized Maxwell model (see text)

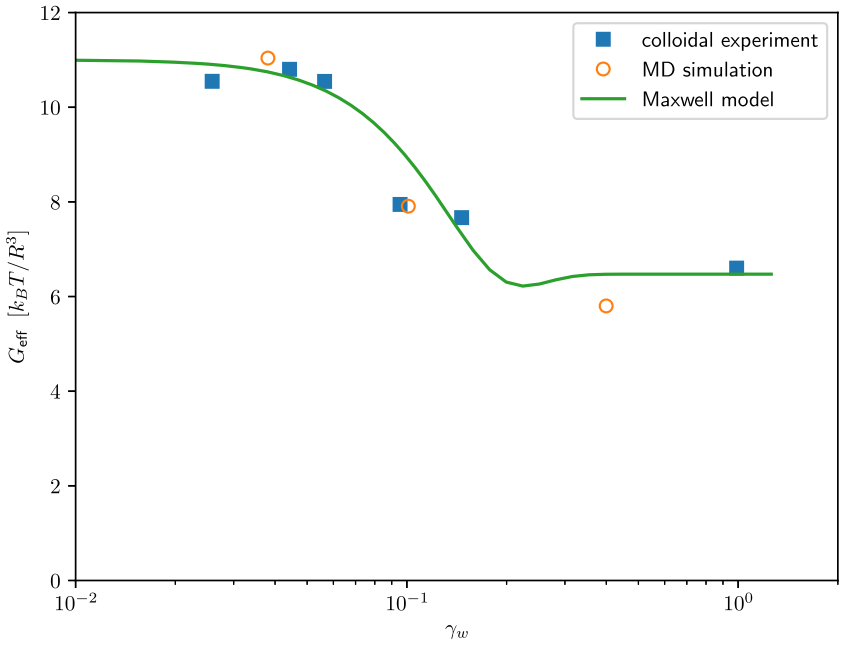

Fig. 7 Filled symbols: Effective shear modulus $G_{\rm eff} = \Delta\sigma/\Delta\gamma$ obtained from the colloidal stress–strain curves shown in Fig. 6. Open symbols: from MD simulations of a typical molecular glass former (data from Ref. [93]). Line: Prediction from a generalized Maxwell model (see text; scaled by 11/15 to match the experimental shear modulus at $\gamma_w = 0$)

in the Green-Kubo integral, a further simplified generalized Maxwell model has been devised [93]. In this model, the shear-induced structural relaxation is approximated by an exponential relaxation decaying on the shear-induced time scale $\dot\gamma$, and the affine advection effect acting on the MCT vertices is modeled by an empirical function. Details of the model are collected in Appendix B. Within the limits of such crude approximations, the generalized Maxwell model predicts the qualitatively correct trend of a reduction in stress overshoot due to pre-strain once $\gamma_w \gtrsim \gamma_c$ (lines in Fig. 6).

From the stress–strain curves at different γ_w, it is suggestive to conclude that also the initial elastic response of the material changes with pre-strain. While a rigorous analysis of the corresponding derivative $d\sigma(\gamma)/d\gamma$ within ITT-MCT is demanding, the generalized Maxwell model offers at least a qualitative description of the effect. From the experimental data, the effective shear modulus as obtained from a finite-difference evaluation, $G_{\rm eff} = \Delta\sigma/\Delta\gamma$ with $\Delta\gamma \lll 0.1$. One observes (symbols in Fig. 7) that the initial shear modulus $G_{\rm eff} \approx 11\,k_BT/R^3$ for $\gamma_w \to 0$, decreases by almost 40% due to pre-strain, and reaches $G_{\rm eff} \approx 7\,k_BT/R^3$ as $\gamma_w \gg \gamma_c$; i.e., the pre-strained material exhibits weaker linear-elastic response. A similar amount of reduction in $G_{\rm eff}$ was found in MD simulations of a typical molecular glass former modeled by a binary truncated-Lennard-Jones mixture (open symbols in Fig. 7, taken from Ref. [93]). The typical strain required to break cages, γ_c, again sets the strain scale over which this reduction in effective shear modulus takes place. The analytical evaluation from the generalized Maxwell model (lines in Fig. 7) confirms this.

Conclusions

We have juxtaposed data on the linear and nonlinear rheologies of metallic melts and colloidal suspensions to shed light on the question to what extent the often quoted "hard-sphere analogy" for the slow relaxation dynamics of disordered hard and soft matter can be made quantitative in the context of linear and nonlinear rheologies. To this end, we have also presented new measurements performed on colloidal model suspensions: confocal microscopy data for PMMA suspensions under startup flow to determine a subtle hexadecupolar deformation mode at the onset of yielding, and time-dependent non-stationary bulk rheology of PS-PNiPAM particles to address specific questions of the history-dependent nonlinear rheology typical of the materials science of metallic glasses.

Our data analysis confirms quantitatively the common qualitative notion that "colloids are big atoms" [1]: The difference in the typical values for the elastic coefficients, GPa in hard matter such as metallic glasses, versus Pa in soft matter, is explained by the different number- and hence energy-density scales due to the different sizes of the relevant constituents.

The base of drawing colloid-vs-atomic analogies is of course a purely dimensional argument for the relevant length and energy scales. We assume that for the stresses, local arrangements are responsible that express predominantly entropic balances caused by the fact that in all the systems we consider, strongly non-overlapping particles are redistributed by thermal fluctuations. Hence, the hard-sphere system is a good model system for dense liquids [33, 94], and energy scales from the direct

interactions between particles cause secondary effects. In fact, in metallic melts, chemical short-range order effects may become interesting, and ultra-soft penetrable particles for example will represent a different system class [95–97].

A key for addressing the mechanisms of yielding and flow of amorphous materials close to the (MCT) glass transition, and to address, e.g., the fate of low-temperature STZ as thermal fluctuations become dominant, is to establish a direct link between microstructural observations and macroscopic rheology. Scattering experiments employing light scattering [98–104] and differential dynamic microscopy [105], X-ray diffraction [77, 106], and small-angle neutron scattering [107] under flow are in principle available. Direct imaging in confocal microscopy under flow [108, 109]—which can also be combined directly with rheometry measurements [110–113]—offers a unique way to extract individual particle positions, also in the flow–gradient plane of shear that is difficult to access in scattering.

Using such tools, it remains a fascinating question to establish the merits and limitations of a unified view on colloidal and bulk-metallic rheology, possibly fixing the boundaries in the deformation–temperature map where different views apply.

Acknowledgments We would like to thank Matthias Ballauff for his continued encouragement to write this paper, and for many useful discussions related to the rheology of colloidal suspensions, and their comparison to metallic alloys, starting from the observation that aspects of creep [69] and of residual stresses [67] that are typical for hard matter solids can be analyzed in great detail in colloidal model suspensions. It was his repeated initiative driving an extremely sluggish environment of coauthors past and present that finally compelled us to put together and finish the analysis that we finally present here. We also thank P. Kuhn for providing the MD simulation data on liquid Ni, and M. Fuchs for his support in the early stages of this project. We thank J. Brillo, A. Meyer, and S. Nell for discussions. The initial part of this work was funded by DFG, Research Unit FOR1394 "Nonlinear Response to Probe Vitrification," projects P1, P2, and P3.

Funding Information Open Access funding provided by Projekt DEAL.

Compliance with ethical standards

Conflict of interest The authors declare that they have no conflict of interest.

Appendix A: Integration through transients and mode-coupling theory of the glass transition (ITT-MCT)

We briefly summarize the main ingredients of the mode-coupling theory of the glass transition (MCT) for the nonlinear rheology of colloidal systems, obtained in the framework of the integration-through transients (ITT) method of calculating non-equilibrium statistical averages. The ITT-MCT was first developed by Fuchs and Cates [114–116], and for a more thorough summary we refer to previous literature [117–119].

ITT starts from an exact reformulation of the Smoluchowski (Fokker-Planck) equation that governs the time evolution of the non-equilibrium probability distribution function of the system. This allows deriving a generalization of the Green-Kubo formula for the stress, relating the non-equilibrium stress $\boldsymbol{\sigma}$ to the shear-rate tensor $\boldsymbol{\kappa}$ and the microscopic stress fluctuations $\hat{\boldsymbol{\sigma}} = -(1/V)\sum_{k=1}^{N}\mathbf{r}_k\mathbf{F}_k$ (for an N-particle system with volume V, particle positions $\mathbf{r}_k$ and interaction forces $\mathbf{F}_k$). One obtains:

$$\boldsymbol{\sigma}(t) = \int_{-\infty}^{t} dt' \beta V \left\langle \boldsymbol{\kappa}(t') : \hat{\boldsymbol{\sigma}} \exp_{-}\left[\int_{t'}^{t} \Omega^{\dagger}(s)\, ds\right]\hat{\boldsymbol{\sigma}}\right\rangle_{\mathrm{eq}}, \qquad (1)$$

where angular brackets indicate *equilibrium* statistical averaging, $\beta = 1/k_BT$ is the Boltzmann factor, and it was assumed that the system was in unstrained quiescent equilibrium in the infinite past. The differential operator $\Omega^{\dagger}$ is the adjoint Smoluchowski operator and includes the nonlinear effects of the deformation history on the dynamics.

The microscopic correlation function that appears under the integral of Eq. 1 is in principle exact, but can only be evaluated after further approximations. In ITT-MCT, one assumes that the dominant stress contributions during structural relaxation arise from microscopic density fluctuations $\delta n_{\mathbf{k}}$ to wave vector $\mathbf{k}$. One defines the transient dynamical density correlation function $\Phi_{\mathbf{k}_{t'}(t)}(t,t') = \left\langle \delta n^{*}_{\mathbf{k}_{t'}(t)} \exp_{-}\left[\int_{t'}^{t}\Omega^{\dagger}(s)\,ds\right]\delta n_{\mathbf{k}}\right\rangle$, where the affine deformation imposed by the homogeneous deformation of the system is taken into account: a density fluctuation $\delta n_{\mathbf{k}}$ at time t originates from an earlier one $\delta n_{\mathbf{k}_0(t)}$ at time 0, where $\mathbf{k}_{t'} = \mathbf{k}\cdot\boldsymbol{F}_{tt'}$. $\boldsymbol{F}_{tt'}$ is the deformation gradient tensor that is known from the finite-strain theory of continuum mechanics. It is related to the velocity-gradient tensor by $\partial_t \boldsymbol{F}_{tt'} = \boldsymbol{\kappa}(t)\cdot\boldsymbol{F}_{tt'}$. After approximations of four-point correlation functions, ITT-MCT arrives at:

$$\boldsymbol{\sigma}/(nk_BT) = -n\int_{-\infty}^{t} dt' \int \frac{d^3k}{32\pi^3}\,[\mathbf{k}\cdot\partial_{t'}\boldsymbol{B}_{tt'}\cdot\mathbf{k}]\,\frac{\mathbf{kk}}{kk_{t'}(t)}c'(k)c'(k_{t'}(t))\Phi_{\mathbf{k}_{t'}(t)}(t,t')^2. \qquad (2)$$

The quantity $c(k)$ is the quiescent-equilibrium direct correlation function that is related to the static structure factor by $S(k) = 1/[1 - nc(k)]$. The Finger tensor (also called left Cauchy-Green tensor) $\boldsymbol{B}_{tt'} = \boldsymbol{F}_{tt'} \cdot \boldsymbol{F}_{tt'}^T$ is the rotation-invariant measure of deformation. In simple shear flow, $-\mathbf{q}_{t'}(t) \cdot \partial_{t'} \boldsymbol{B}_{tt'} \cdot \mathbf{q}_{t'}(t) = \mathbf{q} \cdot \boldsymbol{\kappa}(t') \cdot \mathbf{q}$ reduces to the usual shear rate.

For the evaluation of the transient correlation functions, ITT-MCT provides an evolution equation that takes the form of a nonlinear integro-differential equation. In principle, the full ITT-MCT, including all spatial anisotropies, can be solved [77, 120], but the numerical complexity is rather high. For the results shown in Fig. 5, 2D calculations were thus used, following Refs. [121, 122]. Here, we denote for simplicity only the expressions obtained under an additional isotropic approximation for the wave-vector integrals that has been used to obtain the results shown in Fig. 2. It leads to under the assumption of constant simple shear of rate $\dot{\gamma}$ applied instantaneously at $t \geq 0$, such that the correlation functions also become functions of $t - t'$ only:

$$\sigma_{xy}(t)/(nk_BT) = n\dot{\gamma} \int \frac{k^4\, dk}{60\pi^2} c'(k) c'(k(t)) \Phi_{k(t)}(t)^2 \,, \quad (3)$$

and

$$(1/q^2 D_0)\partial_t \Phi_q(t) + S(q)^{-1} \Phi_q(t) + \int_0^t dt'\, M_q(t-t') \partial_{t'} \Phi_q(t') = 0 \quad (4)$$

with the memory kernel

$$M_q(t) = \frac{n}{2} \int \frac{d^3k}{(2\pi)^3} V_{qkp} V_{qk(t)p(t)} \Phi_k(t) \Phi_p(t) \quad (5)$$

where $p = |\mathbf{q} - \mathbf{k}|$ and $q(t) = q\sqrt{1 + (\dot{\gamma} t/\gamma_c)}$ accounts for the shear advection. The vertices $V_{qkp} = (\mathbf{q} \cdot \mathbf{k}) c(k)/q^2 + (\mathbf{q} \cdot \mathbf{p})/q^2 c(p)$ are given entirely in terms of the equilibrium static structure of the system.

The ITT-MCT model tends to underestimate the decorrelation of fluctuations due to shear; hence, a correction factor γ_c is introduced. The latter is typically taken to be $\gamma_c = 0.1$ in order to match the Lindemann criterion. For the data in Fig. 2, in order to better match the stress overshoots seen in experiment, we adjusted γ_c separately for Eq. 3 (called γ_c') and for Eq. 5.

From the full solutions of the ITT-MCT equations, non-equilibrium averages over microscopic quantities can in principle be calculated, following the derivation of appropriate generalized Green-Kubo relations similar in spirit to Eq. 1 and closures in the spirit of the MCT approximation of the memory kernel. This way, one obtains expressions for the distorted microstructure and hence $\delta g(\mathbf{r})$. For details on these formulas and also the numerical procedure to solve the ITT-MCT equations, we refer to Ref. [121]. The calculations require as physical input the direct correlation functions of the quiescent equilibrium system; we use the standard Percus-Yevick approximation for this to describe a hard-sphere-like system within the theory.

Appendix B: Generalized Maxwell model

Based on a schematically simplified version of the generalized ITT-MCT Green-Kubo-like formula for the stress, Eq. 3, under simple shear geometry:

$$\sigma_{xy} = \int_{-\infty}^{t} \dot{\gamma}(t') v_\sigma(\gamma_{tt'}) G(t, t', [\dot{\gamma}]) \,, \quad (6)$$

a generalized Maxwell model was proposed [22, 123] to provide a model that captures a number of qualitative predictions of the full ITT-MCT and at the same time lends itself to a more rigorous analytical analysis. Based on Maxwell's model of viscoelasticity [124], and approximating the shear-induced structural relaxation rate $1/\tau \sim 1/\tau_{\rm eq} + |\dot{\gamma}|/\gamma_c$, one assumes the dynamical shear modulus to decay exponentially at long times. Assuming further the quiescent system to be effectively frozen in, one sets:

$$G(t, t', [\dot{\gamma}]) \simeq G_\infty \exp\left[-(t - t')|\dot{\gamma}|/\gamma_c\right] . \quad (7)$$

For our analysis of the Bauschinger effect, this relaxation behavior is obtained for all times because, due to symmetry constraints, only the magnitude of the applied shear rate can enter the dynamical shear modulus. The vertex function is further approximated by an ad hoc functional form that captures the decay to zero with increasing strain and exhibits an undershoot that gives rise to a stress overshoot under startup flow:

$$v_\sigma(\gamma) = \left(1 - (\gamma/\gamma_*)^2\right) \exp\left[-(\gamma/\gamma_{**})^2\right] . \quad (8)$$

Here, γ_* and γ_{**} are tunable parameters that play the role of γ_c but differ in their numerical values in order to capture the effect that, in determining the stress overshoot, density fluctuations of slightly different wave length decorrelate on slightly different strain scales; an effect that is necessarily missing in a simplified model that ignores the spatial resolution of density fluctuations. A modified variant of $v_\sigma(\gamma)$ employing fourth powers of γ was used to rationalize startup flow in schematic ITT-MCT models [60]; here, we use a simpler version that includes a strictly quadratic strain dependence in $v_\sigma(\gamma)$. It allows integrating the expressions for the Bauschinger effect analytically, at the cost of giving quantitatively less accurate fits of the experimental data.

For the results of the generalized Maxwell model shown in Fig. 6, we used $G_{\rm eff} = 15$, $\gamma_c = 0.14$, $\gamma_* = 0.1$, and $\gamma_{**} = 0.125$ at a shear rate given by the bare Péclet number $\dot{\gamma}\tau_0 = 5 \times 10^{-4}$. This gives reasonable fits of the

experimental data, but it overestimates G_∞; in Fig. 7, this effect was scaled out.

Appendix C: Simulation details

Molecular-dynamics (MD) simulations were performed for a system of liquid Ni. These simulations employ an embedded-atom method (EAM) potential proposed by Foiles [125] that was gauged against experimental data for the liquid state of Ni. The same model has been used previously to study crystal growth in metallic melts [126–128]; we refer the reader to these references for further details on the interaction potential. Simulations with $N = 8788$ particles in the NVT ensemble using Lees-Edwards boundary conditions to impose simple shear, and a DPD thermostat to maintain a temperature of $T = 1400\,\mathrm{K}$ were employed. This represents a strongly undercooled state; the melting temperature of the MD system is $T_m \approx 1748\,\mathrm{K}$. Shear was applied to match a dressed Péclet (Weissenberg) number $Pe = \dot\gamma\tau \approx 1$.

For simulations of a sheared hard-sphere system undergoing Brownian motion, we employed an event-driven algorithm [129]. In these BD simulations, a binary equimolar mixture of $N = 1000$ particles with size ratio 1.4 is used as a system whose glass-transition dynamics has been extensively studied. Simulations are performed at $\varphi = 0.81$, slightly above the MCT transition point of the system, $\varphi_c \approx 0.795$. The shear rate of $\dot\gamma = 2 \times 10^{-3}/\tau_0$ is applied via Lees-Edwards boundary condition; the corresponding dressed Péclet number $Pe \gg 10$. For the evaluation of stress and pair-distribution values, see Ref. [130]. For $\delta g(r)$, the correlations between big particles were evaluated; it is not qualitatively different from the other partial $g(r)$ in this mixture.

Appendix D: Confocal microscopy under shear

For colloidal microscopy, dispersions of polymethylmethacrylate (PMMA) colloids stabilized with polyhydroxystearic acid and flourescently labeled with nitrobenzoxadiazole in a solvent mixture of cycloheptyl bromide and cis-decalin (to provide both density and refractive-index matching) with addition of 4 mM tetrabutylammoniumchloride were prepared. The dispersed particles display hard-sphere behavior to a good extent [71] and have an average radius $R \approx 780\,\mathrm{nm}$ (6% polydispersity). A volume fraction of $\varphi \approx 0.565$ was used, just below the expected glass transition at $\varphi_g \approx 0.58$. Shear is applied corresponding to a dressed Péclet number $Pe \approx 144$, by means of a home-built shear cell employing two parallel plates covered with PMMA particles to avoid wall slip [26, 27, 73, 99].

Prior to the measurements, the samples are exposed to oscillatory shear (exceeding 100% strain for 10 cycles at a frequency below 0.1 Hz) following a rest period of 600 s.

Confocal microscopy is performed with a VT-Eye confocal microscope (Visitech International) mounted on a Nikon Ti-U inverted microscope. Image stacks are acquired at a depth of 15 μm into the sample, using a Nikon Plan Apo VC 100× oil immersion objective. An image stack of $512 \times 512 \times 50$ pixels corresponds to a volume of $51 \times 51 \times 10\,\mu\mathrm{m}^3$, and contains around 8500 particles. Coordinates are extracts using standard routines [131] and refined [29]. The data for $g(\mathbf{r})$ are averaged over ten experiments, counting particles within a slice of thickness $2.8R$ in the velocity-gradient plane around each reference particle.

Projections onto spherical harmonics in 3D are defined by

$$g(\mathbf{r}) = \sum_{l=0}^{\infty} \sum_{m=-l}^{l} g_{lm}(r) Y_{lm}(\theta, \phi)\,, \tag{9}$$

and the relevant $l = 2$ and $l = 4$ terms in the 2D plane have coefficients

$$g_{22}(r) = \frac{1}{2}\sqrt{\frac{15}{2\pi}} \int d\Omega\; g(\mathbf{r}) \sin\theta \cos\theta\, (\sin\phi)^2\,, \tag{10}$$

$$g_{44}(r) = \frac{3}{16}\sqrt{\frac{35}{2\pi}} \int d\Omega\; g(\mathbf{r}) \cos 4\theta\, (\sin\phi)^4\,. \tag{11}$$

This follows the convention of Ref. [132] but differs slightly from the one used elsewhere [133].

References

1. Poon WCK (2004) Science 304:830
2. Poon WCK (2016) J Phys A 49:401001
3. Terentjev EM, Weitz DA (eds) (2015) The Oxford Handbook of Soft Condensed Matter. Oxford University Press, Oxford
4. Dhont JKG (2003) An introduction to dynamics of colloids, 2nd edn. Elsevier, Amsterdam
5. Götze W (2009) Complex dynamics of Glass-Forming liquids. Oxford university press, Oxford
6. Bouchbinder E, Langer JS (2011) Phys Rev Lett 106:148301
7. Hunter GL, Weeks ER (2012) Rep Prog Phys 75(6):066501
8. Gleim T, Kob W, Binder K (1998) Phys Rev Lett 81:4404
9. Szamel G, Flenner E (2004) EPL 67:779
10. Weeks ER, Weitz DA (2002) Phys Rev Lett 89:095704
11. Szamel G, Löwen H (1991) Phys Rev A 44:8215
12. Mandal S, Franosch T, Voigtmann Th (2018) Soft Matter 14:9153
13. Spanner M, Höfling F, Kapfer SC, Mecke KR, Schröder-Turk GE, Franosch T (2016) Phys Rev Lett 116:060601
14. Schuh CA, Hufnagel TC, Ramamurty U (2007) Acta Mater 55:4067
15. Kato H, Kawamura Y, Inoue A (1998) Appl Rev Lett 73:3665
16. Rodney D, Tanguy A, Vandembroucq D. (2011) Modelling Simul Mater Sci Eng 19:083001

17. Johnson WL, Samwer K (2005) Phys Rev Lett 95:195501
18. Schall P, Weitz DA, Spaepen F (2007) Science 318:1895
19. Chikkadi VK, Wegdam G, Bonn D, Nienhuis B, Schall P (2011) Phys Rev Lett 107:198303
20. Falk ML, Langer JS (2011) Annu Rev Cond Matt Phys 2:353
21. Fuchs M, Ballauff M (2005) J Chem Phys 122:094707
22. Fuchs M, Ballauff M (2005) Colloids Surf A 270:232
23. Crassous JJ, Siebenbürger M, Ballauff M, Drechsler M, Henrich O, Fuchs M (2006) J Chem Phys 125:204906
24. Crassous JJ, Siebenbürger M, Ballauff M, Drechsler M, Hajnal D, Henrich O, Fuchs M (2008) J Chem Phys 128:204902
25. Siebenbürger M, Fuchs M, Winter H, Ballauff M (2009) J Rheol 53:707
26. Besseling R, Weeks ER, Schofield AB, Poon WCK (2007) Phys Rev Lett 99:028301
27. Zausch J, Horbach J, Laurati M, Egelhaaf SU, Brader JM, Voigtmann Th, Fuchs M (2008) J Phys Condens Matter 20:404210
28. Cheng X, McCoy JH, Israelachvili JN, Cohen I (2011) Science 333:1276
29. Jenkins MC, Egelhaaf SU (2008) Adv Colloid Interf Sci 136:65
30. Meyer A (2002) Phys Rev B 66:134205
31. Pusey PN, van Megen W (1986) Nature (London) 320:340
32. Miracle DB, Louzguine-Luzgin D, Louzguina-Luzgina L, Inoue A (2010) Int Mater Rev 55:218
33. Bernal JD (1959) Nature 183:141
34. Pauling L (1947) Chem J Am Soc 69:542
35. Brillo J, Pommrich AI, Meyer A (2011) Phys Rev Lett 107:165902
36. Peng HL, Yang F, Liu ST, Holland-Moritz D, Kordel T, Hansen T, Voigtmann Th (2019) Phys Rev B 100:104202
37. Jonas I (2017) Thermophysical and structural properties of the equilibrium and undercooled melt of bulk metallic glasses investigated by electrostatic levitation. Ph.D. Thesis University of Saarbrücken, Germany
38. Russel WB, Wagner NJ, Mewis J (2013) J Rheol 57:1555
39. Peng HL, Voigtmann Th, Kolland G, Kobatake H, Brillo J (2015) Phys Rev B 92:184201
40. Maret M, Pomme T, Pasturel A, Chieux P (1990) Phys. Rev. B 42:1598
41. Das SK, Horbach J, Koza MM, Mavila Chatoth S, Meyer A (2005) Appl Phys Lett 86:011918
42. Yuan CC, Yang F, Kargl F, Holland-Moritz D, Simeoni GG, Meyer A (2015) Phys Rev B 91:214203
43. Krausser J, Samwer KH, Zaccone A (2015) Proc Natl Acad Sci (USA) 112:13762
44. Imhof A, Dhont JKG (1995) Phys Rev Lett 75:1662
45. Imhof A, Dhont JKG (1995) Phys Rev E 52:6344
46. Moreno AJ, Colmenero J (2006) Phys Rev E 74:021409
47. Moreno AJ, Colmenero J (2006) J Chem Phys 125:164507
48. Mayer C, Stiakakis E, Zaccarelli E, Likos CN, Sciortino F, Tartaglia P, Löwen H, Vlassopoulos D (2007) Rheol Acta 46:611
49. Mayer C, Zaccarelli E, Stiakakis E, Likos CN, Sciortino F, Munam A, Gauthier M, Hadjichristidis N, Iatrou H, Tartaglia P, Löwen H, Vlassopoulos D (2008) Nat Mater 7:780
50. Hendricks J, Capellmann R, Schofield AB, Egelhaaf SU, Laurati M (2015) Phys Rev E 91:032308
51. Sentjabrskaja T, Zaccarelli E, De Michele C, Sciortino F, Tartaglia P, Voigtmann Th, Egelhaaf SU, Laurati M (2016) Nature Commun 7:11133
52. Götze W, Voigtmann Th (2003) Phys Rev E 67:021502
53. Voigtmann T (2011) EPL 96:36006
54. Lázaro-Lázaro E, Perera-Burgos JA, Laermann P, Sentjabrskaja T., Pérez-Ángel G, Laurati M, Egelhaaf SU, Medina-Noyola M, Voigtmann T, Castañeda-Priego R, Elizondo-Aguilera LF (2019) Phys. Rev. E 99:042603
55. T. Sentjabrskaja, Babaliari E, Hendricks J, Laurati M, Petekidis G, Egelhaaf SU (2013) Soft Matter 9:4524
56. Sentjabrskaja T, Hermes M, Poon WCK, Estrada CD, Castañeda-Priego R, Egelhaaf SU, Laurati M (2014) Soft Matter 10:6546
57. Sentjabrskaja T, Jacob AR, Egelhaaf SU, Petekidis G, Voigtmann T, Laurati M (2019) Soft Matter 15:2232
58. Foffi G, Götze W, Sciortino F, Tartaglia P, Voigtmann T (2003) Phys Rev Lett 91:085701
59. Lu J, Ravichandran G, Johnson WL (2003) Acta Mater 51:3429
60. Amann CP, Siebenbürger M, Krüger M, Weysser F, Fuchs M (2013) J Rheol 57:149
61. Lindemann FA (1910) Phys Z 11:609
62. Yu HB, Richert R, Maaß R, Samwer K (2015) Phys Rev Lett 115:135701
63. Koumakis N, Laurati M, Egelhaaf SU, Brady JF, Petekidis G (2012) Phys Rev Lett 108:098303
64. Koumakis N, Laurati M, Jacob AR, Mutch KJ, Abdellali A, Schofield AB, Egelhaaf SU, Brady JF, Petekidis G (2016) J Rheol 60:603
65. Brader JM, Voigtmann Th, Fuchs M, Larson RG, Cates ME (2009) Proc Natl Acad Sci USA 106:15186
66. Lemaître A (2015) J Chem Phys 143:164515
67. Ballauff M, Brader JM, Egelhaaf SU, Fuchs M, Horbach J, Koumakis N, Krüger M, Laurati M, Mutch KJ, Petekidis G, Siebenbürger M, Voigtmann T, Zausch J (2013) Phys Rev Lett 110:215701
68. Laurati M, Maßhoff P, Mutch KJ, Egelhaaf SU, Zaccone A (2017) Phys Rev Lett 118:018002
69. Siebenbürger M, Ballauff M, Voigtmann Th (2012) Phys Rev Lett 108:255701
70. Jacob AR, Moghimi E, Petekidis G (2019) Phys Fluids 31:087103
71. Royall CP, Poon WCK, Weeks ER (2013) Soft Matter 9:17
72. Koumakis N, Pamvouxoglou A, Poulos AS, Petekidis G (2012) Soft Matter 8:4271
73. Laurati M, Mutch KJ, Koumakis N, Zausch J, Amann CP, Schofield AB, Petekidis G, Brady JF, Horbach J, Fuchs M, Egelhaaf SU (2012) Phys J Condens Matter 24:464104
74. Carrier V, Petekidis G (2009) J Rheol 53:245
75. Voigtmann Th, Meyer A, Holland-Moritz D, Stüber S, Hansen T, Unruh T (2008) EPL 82:66001
76. Nowak B, Holland-Moritz D, Yang F, Voigtmann Th, Kordel T, Hansen TC, Meyer A (2017) Phys Rev Materials 1:025603
77. Amann CP, Denisov D, Dang MT, Struth B, Schall P, Fuchs M (2015) J Chem Phys 143:034505
78. Besseling R, Isa L, Ballesta P, Petekidis G, Cates ME, Poon WCK (2010) Phys Rev Lett 105:268301
79. Mandal S, Gross M, Raabe D, Varnik F (2012) Phys Rev Lett 108:098301
80. Fielding SM (2014) Rep Prog Phys 77:102601
81. Voigtmann T (2014) Curr Opin Colloid Interf Sci 19:549
82. Chikkadi V, Miedema DM, Dang MT, Nienhuis B, Schall P (2014) Phys Rev Lett 113:208301
83. Brader JM, Cates ME, Fuchs M (2012) Phys Rev E 86:021403
84. Bucknall CB (1977) Toughened Plastics. Materials science series. Springer Science+Business Media, Dordrecht
85. Ward IM, Sweeney J (2013) Mechanical properties of solid polymers, 3rd edn. Wiley & Sons, West Sussex
86. Cohen-Addad S, Höhler R, Pitois O (2013) Annu Rev Fluid Mech 45:241
87. Desmond KW, Weeks ER (2015) Phys Rev Lett 115:098302
88. Hutzler S, Weaire D (2011) Colloids Surf A 382:3
89. Dennin M (2004) Phys Rev E 70:041406

90. Tsamados M, Tanguy A, Goldenberg C, Barrat JL (2009) Phys Rev E 80:026112
91. Bauschinger J (1886) Mittheilungen Mech-techn Lab der kgl Techn Hochschule Mü,nchen 13:1
92. Karmakar S, Lerner E, Procaccia I (2010) Phys Rev E 82:026104
93. Frahsa F, Bhattacharjee AK, Horbach J, Fuchs M, Voigtmann T (2013) J Chem Phys 138:12A513
94. Widom B (1967) Science 157:375
95. Ikeda A, Berthier L, Sollich P (2012) Phys Rev Lett 109:018301
96. Ikeda A, Berthier L, Sollich P (2013) Soft Matter 9:7669
97. Bonn D, Denn MM, Berthier L, Divoux T, Manneville S (2017) Rev Mod Phys 89:035005
98. Matsuzaka K, Hashimoto T (1999) Rev Sci Inst 70:2387
99. Petekidis G, Pusey PN, Moussaïd A, Egelhaaf S, Poon WCK (2002) Physica A 306:334
100. Laurati M, Egelhaaf SU, Petekidis G (2014) J Rheol 58:1395
101. Ali N, Roux DCD, Cipelletti L, Caton F (2016) Meas Sci Technol 27:125902
102. Aime S, Ramos L, Fromental JM, Prévot G, Jelinek R, Cipelletti L (2016) Rev Sci Inst 87:123907
103. Aime S, Cipelletti L (2019) Soft Matter 15:200
104. Pommella A, Philippe AM, Phou T, Ramos L, Cipelletti L (2019) Phys Rev Applied 11:034073
105. Aime S, Cipelletti L (2019) Soft Matter 15:213
106. Leheny RL, Rogers MC, Chen K, Narayanan S, Harden JL (2015) Curr Opin Colloid Interf Sci 20:261
107. Calabrese MA, Wagner NJ (2017). In: Dreiss CA, Feng Y (eds) Wormlike Micelles. The Royal Society of Chemistry, London, pp 193–235
108. Wu YL, Brand JHJ, van Gemert JLA, Verkerk J, Wisman H, va Blaaderen A, Imhof A (2007) Rev Sci Inst 78:103902
109. Boitte JB, Vizcaíno C, Benyahia L, Herry JM, Michon C, Hayert M (2013) Rev Sci Inst 84:013709
110. Lin NYC, McCoy JH, Cheng X, Leahy B, Israelachvili JN, Cohen I (2014) Rev Sci Inst 85:033905
111. Sentjabrskaja T, Hermes M, Poon WCK, Estrada CD, Castañeda Priego R, Egelhaaf SU, Laurati M (2014) Soft Matter 10:6546
112. Sentjabrskaja T, Chaudhuri P, Hermes M, Poon WCK, Horbach J, Egelhaaf SU, Laurati M (2015) Sci Rep 5:11884
113. Colombo G, Massaro R, Coleman S, Läuger J, Van Puyvelde P, Vermant J (2019) Korea-Aust Rheol J 31:229
114. Fuchs M, Cates ME (2002) Phys Rev Lett 89:248304
115. Brader JM, Voigtmann T, Cates ME, Fuchs M (2007) Phys Rev Lett 98:058301
116. Brader JM, Cates ME, Fuchs M (2008) Phys Rev Lett 101:138301
117. Fuchs M (2010) Adv Polym Sci 236:55
118. Brader JM (2010) J Phys Condens Matter 22:363101
119. Nägele G, Dhont JKG, Voigtmann Th (2020). In: Wagner NJ, Mewis J (eds) Theory and Applications of Colloidal Suspension Rheology. Cambridge University Press, Cambridge
120. Amann CP, Siebenbürger M, Ballauff M, Fuchs M (2015) Phy J Condens Matter 27:194121
121. Henrich O, Weysser F, Cates ME, Fuchs M (2009) Philos Trans R Soc London A 367:5033
122. Krüger M, Weysser F, Fuchs M (2011) Eur Phys J E 34:88
123. Papenkort S, Voigtmann T (2015) J Chem Phys 143:044512
124. Maxwell JC (1867) Philos Tans R Soc London 157:49
125. Foiles SM (1985) Rev Phys B 32:3409
126. Zykova-Timan T, Rozas RE, Horbach J, Binder K (2009) J Phys Condens Matter 21:464102
127. Rozas RE, Horbach J (2010) EPL 93:26006
128. Rozas RE, Horbach J (2012). In: Herlach DM, Matson DM (eds) Solidification of Containerless Undercooled Melts. Wiley-VCH, Weinheim, pp 381–401
129. Scala A, Voigtmann Th, De Michele C (2007) J Chem Phys 126:134109
130. Brady JF, Morris JF (1997) J Fluid Mech 348:103
131. Crocker JC, Grier DG (1996) J Colloid Interface Sci 179:298
132. Strating P (1999) Phys Rev E 59:2175
133. Zausch J, Horbach J (2009) EPL 88:60001

Thomas Voigtmann obtained his PhD in theoretical physics from the TU Munich in 2003, and currently is head of the Theory and Simulation group of the Institute of Materials Physics in Space at DLR, and Professor of Soft Matter Theory at the University of Düsseldorf. He works on the dynamics and rheology of colloidal suspensions out of equilibrium and of active-matter models, combining microscopic and macroscopic theory, simulations, and (where plausible) experiments under microgravity conditions.

Matthias Ballauff has been a constant mentor for me since our fruitful collaboration on creep and residual stresses jointly with Miriam Siebenbürger. I always sincerely enjoyed working and discussing science and non-science with you, Matthias, and I dearly remember our wondering why progress sometimes really creeps and why "The Gorilla" story of residual stresses caused more attention than our other work. It is my great pleasure to finally keep the promise regarding "the metal analogy."

Miriam Siebenbürger conducted her PhD research with Matthias Ballauff in Bayreuth. Her research focused on the rheology of dense colloidal suspensions. After completing her PhD in2011, she continued working with Matthias Ballauff as a research scientist, but then moved to LSU CAMD in Baton Rouge, Louisiana, where she is a beamline scientist.

Dear Matthias, as an inspiring mentor, you introduced me to the field of colloids, rheology, and soft matter which instantly became my scientific passion. You allowed me to grow, gather expertise, and build up the broad background I possess today, taking the German word "Doktorvater" (= PhD father) literally. With the persistence of the ancient Roman senator, Cato the Older, you encouraged us to concentrate on what remained to be published in this area—the comparison of colloidal and metal glasses. So, here it is! Happy Birthday! With best wishes for a happy and productive "retirement."

Stefan U. Egelhaaf obtained his PhD from the ETH Zürich in 1995. Subsequently, he worked at the Institute Laue-Langevin in Grenoble and The University of Edinburgh from where he moved to the Heinrich Heine University in Düsseldorf to take up his current position as Chair of Soft Matter Physics. He is interested in colloidal suspensions under non-equilibrium conditions, for example under shear or in external potentials. He investigates their microscopic structure and dynamics as well as their macroscopic bulk behavior using scattering and microscopy techniques and rheological measurements.

The work of Matthias Ballauff has been a constant source of inspiration to me, his publications, as well as his talks, and in particular the personal discussions with him. At the many occasions I could discuss and exchange ideas with him, I always greatly benefited from his broad knowledge, understanding, and intuition, for which I am very grateful to him.

Konrad Samwer and Matthias Ballauff have been colleagues for many years. Konrad Samwer says: We have discussed the "metal analogy" for so long but never really put it together. I remember very much our meeting in Hefei in 2015, where we had every breakfast and dinner time for extra rounds of arguments for and against a close relationship of the BMG's and colloidal systems or polymers. Now we are both retired and this work is just the beginning, Matthias. Let's keep going, and may our curiosity never end. Thank you very much. Konrad.